



Influence of Maximum Curvature Position of Airfoil on Aerodynamic Characteristics of Aircraft Under Low Reynolds Number Conditions

Zeyang Cai

Detroit Green Technology Institute, Hubei University of Technology, Wuhan, 430000, China

2211611224@hbut.edu.cn

Abstract. In recent years, in high-altitude long-time navigation, UAVs have attracted much attention due to their advantages of long-range and unmanned working characteristics. The working environment of this kind of UAV is thin, which often leads to this kind of aircraft being in an environment with a low Reynolds number. This article sets the flight speed to 10m/s and the Reynolds number to $6.8e+5$ for comparative analysis of different airfoils at the maximum position. Use ANSYS Fluent fluid simulation to solve and calculate the geometric model and mesh division of airfoils. Simulate and calculate using the K-SST turbulence model and pressure-based solver. By selecting the common two-dimensional models of NACA2312 and NACA2412 to reduce computational complexity, it is possible to quickly simulate airfoils with different curvature positions through both simulations. By comparing and analyzing the lift coefficient, drag coefficient, pressure cloud map, and velocity cloud map of NACA2312 and NACA2412, reference can be provided for the selection of airfoils for low-speed aircraft and aircraft takeoff and landing at low Reynolds numbers.

Keywords: Aerodynamic Characteristics, Naca Airfoil, CFD Simulation

1 Introduction

In the aerospace field, the study of aerodynamic characteristics of airfoils has always been one of the core topics. The performance of the airfoil directly affects key parameters such as lift, drag, stability, and maneuverability of the aircraft.

Reynolds number is a dimensionless number that can be employed to characterize fluid flow, representing the ratio of inertial and viscous force levels in physics. Low Reynolds number flow typically occurs in low-speed, UAV, and high-altitude flight scenarios. Under these conditions, the viscous effect of the fluid is relatively significant, and the phenomenon of flow separation is more likely to occur, thereby significantly affecting the aerodynamic performance of the airfoil.

Traditional airfoil research requires searching for hollow laboratories for simulation, which incurs significant time and financial costs. The Ansys Fluent

simulation used in this study can effectively compensate for this by efficiently and cost-effectively supplementing the aerodynamic characteristics of airfoils in the low Reynolds number field.

This study mainly used ANSYS Fluent fluid simulation software to simulate and analyze two different curvature airfoils under low Reynolds number conditions. It also simulated the lift coefficient, drag coefficient, pressure, and velocity distribution cloud maps at five different angles of attack to draw conclusions. Through the combination of experimental measurement and numerical simulation, it provides a reference for the optimization and invention of airfoils at low Reynolds numbers [1-3].

2 Methodology

2.1 Airfoil Selection

The airfoils selected for this study are NACA2312 and NACA2412, as shown in Fig. 1. The data coordinates of the two airfoils are obtained through the airfoil plotter, using 200-node mesh closed curves with a chord length of 1 meter.

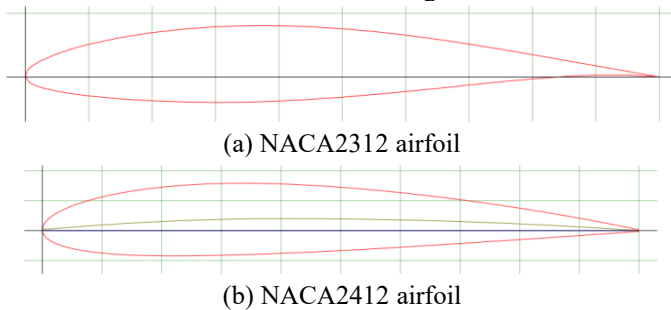


Fig. 1. Coordinate diagram of NACA2312 and NACA2412. (Picture credit: Original)

2.2 Grid Generation

Before grid generation, the calculation domain is defined. Fig.2 shows the range of calculation domains used for simulation. The chord length is set to one meter, and the length of the calculation domain is 15 meters. Set the right side of the calculation domain as the pressure outlet and the remaining side as the velocity inlet.

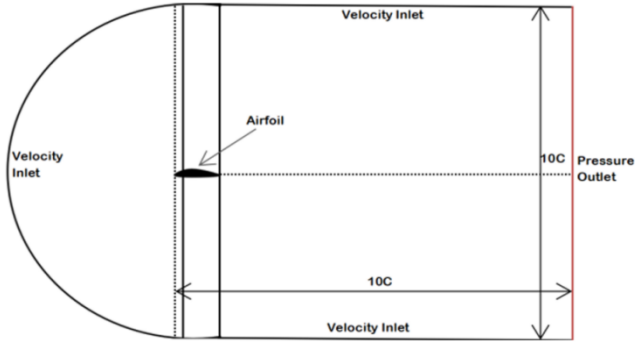
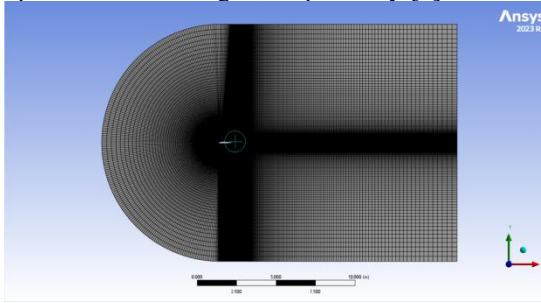
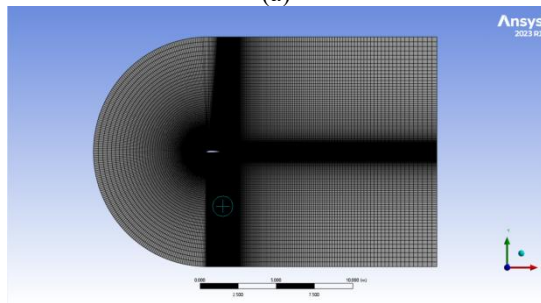


Fig. 2. The range of calculation domains [4]

Generate computational domain grids for NACA2312 and NACA2412 using the range of the computational domain. Fig. 3 and Fig. 4 are the approximate and detailed diagrams of the computational domain grid, respectively [5].



(a)



(b)

Fig. 3. The computational domain grid diagram of (a) NACA2312 and (b) NACA2412 (Picture credit: Original)

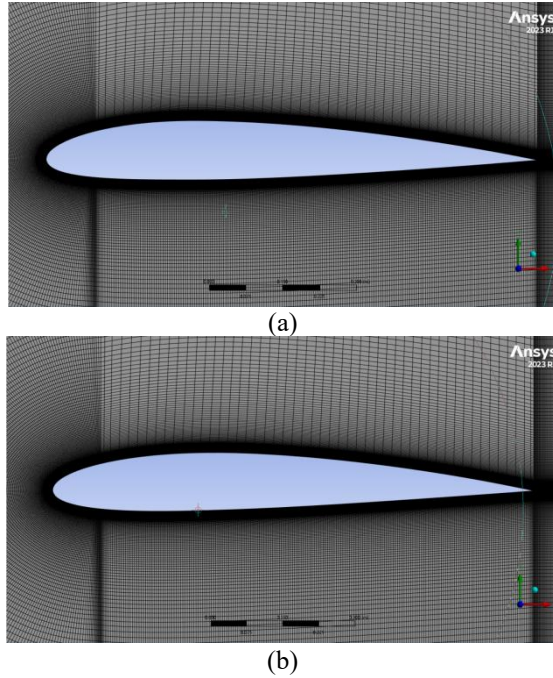


Fig. 4. A detailed diagram of the computational domain grid of (a) NACA2312 and (b) NACA2412 (Picture credit: Original)

2.3 Boundary Conditions and Governing Equations

Boundary conditions refer to the physical properties or conditions on the surface of a computational domain, representing specific flow variables of a physical model. To obtain more accurate numerical results, 500 iterations, and $1e-5$ iteration errors were set in the CFD simulation to ensure that the error of the results is less than $1e-5$ [6] (Table 1).

Table 1. Fluent details

Solver	Pressure based steady
Viscous Model	K- ω SST model
Turbulence intensity ratio	0.1
Viscosity(kg/m-s)	1.79e-05
Density(kg/m ³)	1.23
Turbulence length scale	0.3
Chord length(m)	1
Reynolds Number	6.8e+5
Inlet Velocity(m/s)	10
Momentum	Second Order Upwind
Pressure velocity coupling	Coupled

The basic governing equations used in this paper are the incompressible continuity equation and the Navier-Stokes equation. The continuity equation is expressed as follows:

$$\frac{\partial \rho}{\partial t} + \frac{\partial \rho u}{\partial x} + \frac{\partial \rho v}{\partial y} + \frac{\partial \rho w}{\partial z} = 0 \quad (1)$$

Where, u , V , and W are velocity components of fluid in X , y , and Z directions respectively. The formula ensures the continuity of airflow and mass conservation.

The Navier-Stokes equation is expressed as follows:

$$\rho \frac{\partial v}{\partial t} + \rho((V \cdot \nabla)V) = -\nabla p + \rho g + \nabla \cdot \tau \quad (2)$$

The first item is divided into two parts. The first part is the fluid density ρ . The partial derivative of velocity V at time t in the second part represents the rate at which fluid velocity changes over time. $\rho(V \cdot \nabla)V$ is the inertia term. $-\nabla p$ is the pressure gradient, ρg is the effect of gravitational acceleration, $\nabla \cdot \tau$ is the divergence of viscous stress. By solving this equation, the velocity field and pressure field of the fluid can be obtained, and the aerodynamic performance of the airfoil can be analyzed [7].

3 Results

This article uses Ansys Fluent fluid simulation software to simulate NACA2312 and NACA2412 based on the grid diagram and environmental settings mentioned above and sets the angle of attack between $0-12^\circ$ to obtain cloud maps of lift, drag coefficient, pressure, and velocity distribution [8].

3.1 Comparative Analysis of Lift Coefficient and Drag Coefficient at $0-12^\circ$ Angle of Attack (AOA)

Fig.5 shows the lift coefficient comparison diagram of naca2312 and naca2412 in the diversity of $0-12^\circ$ AOA. In the figure, there is no stall, the lift coefficient still shows a linear growth trend, and the lift coefficient of NACA2412 is better than that of NACA2312. According to Bernoulli's principle, the greater the difference in pressure between the upper and lower surfaces, the overall lift coefficient of the airfoil will increase. NACA2412 has a larger curvature, more obvious upper surface curvature, and stronger acceleration when airflow passes through. The maximum camber ranges from 30% to 40%. The position of the maximum curvature on the airfoil moves backward, resulting in NACA2412 having a slightly lower value than NACA2312 at 12° . From the comparison in the figure, the slope of NACA2412 is steeper [9].

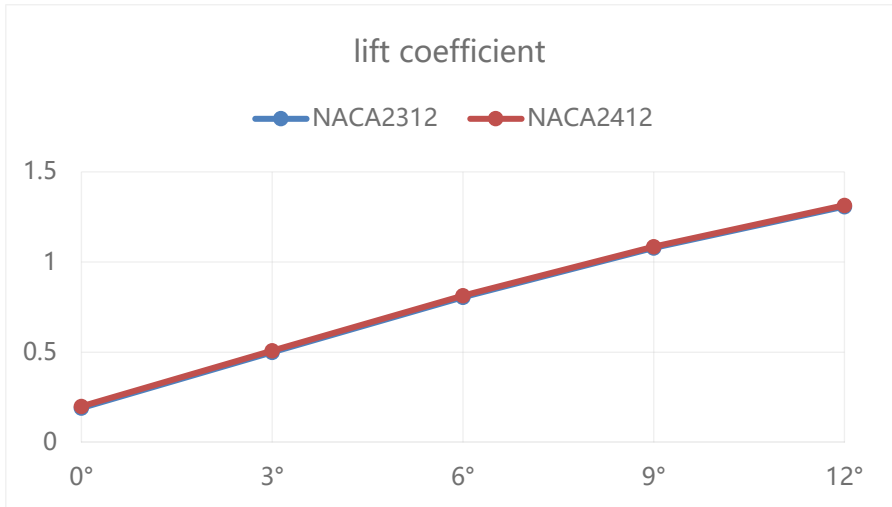


Fig. 5. Lift coefficient of NACA2312 and NACA2412 (Picture credit: Original)

Fig. 6 shows a comparison of drag coefficients between NACA2312 and NACA2412 within the AOA range of 0-12°. At AOA of 0-9°, the drag coefficient of NACA2412 is slightly higher than that of NACA2312. At angles of attack of 9° -12°, the drag coefficient of NACA2312 will be greater than that of NACA2412. The backward movement of the curvature position slows down the pressure differential resistance, making the growth trend of resistance smoother.

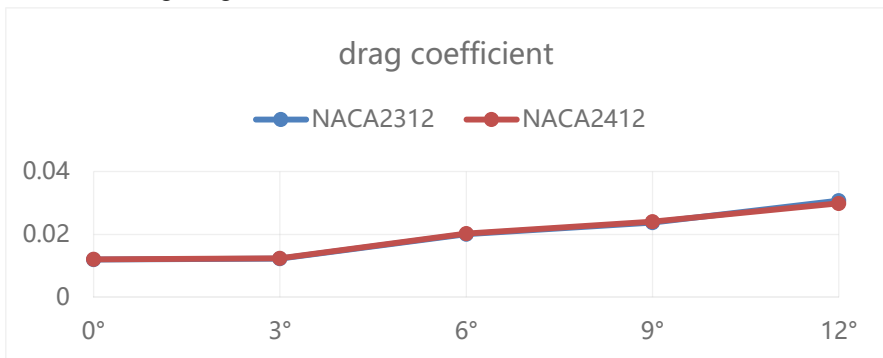


Fig. 6. drag coefficient of NACA2312 and NACA2412 (Picture credit: Original)

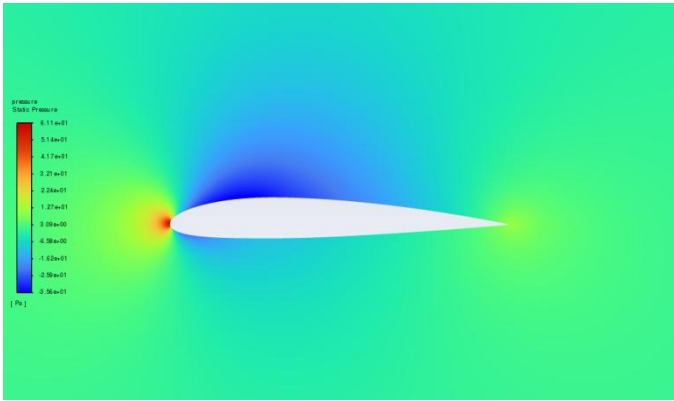
3.2 Comparison of Pressure Distribution Cloud Maps and Velocity Distribution Cloud Maps within Different Attack Angle Ranges

Figs. 7 and 8 are pressure distribution programs of NACA2312 and NACA2412, respectively.

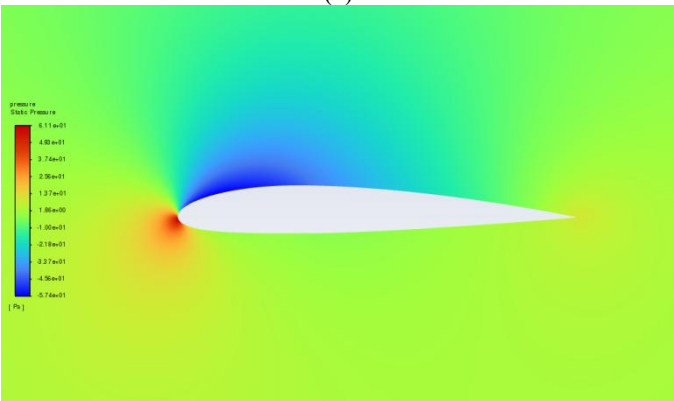
In Fig. 7, NACA2312 approaches stall at 12 °. At low angles of attack, resistance is mainly generated by friction. At high angles of attack, resistance is mainly generated by pressure differences.

In Fig. 8, At an angle of attack of 0-6 °, the lift is good and the flow adhesion is strong. At an AOA of 9-12 °, NACA2412 gradually stalls, causing a rapid increase in drag and a collapse of lift.

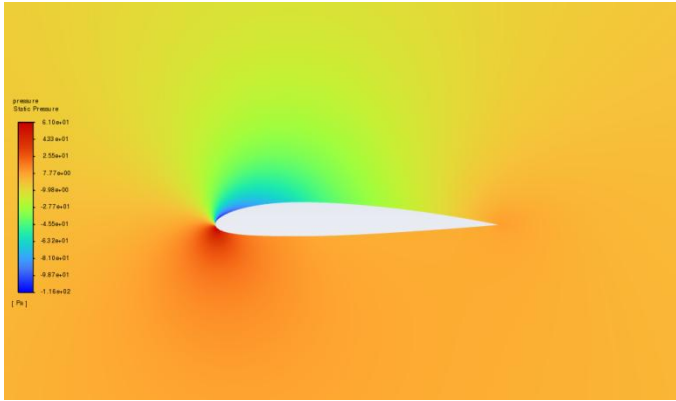
In the pressure distribution cloud map, the low-pressure area of NACA2312 is small and forward, with a gentle change in pressure gradient and slower collapse after stall. The low-pressure area of NACA2412 is large and located further back, with a steep pressure gradient, and the low-pressure area suddenly disappears during stall [10].



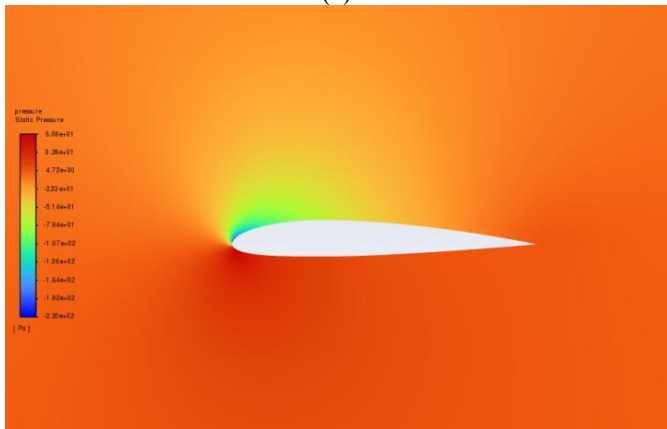
(a)



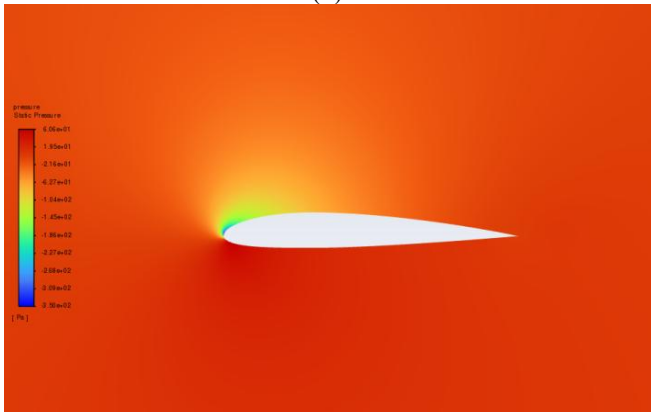
(b)



(c)

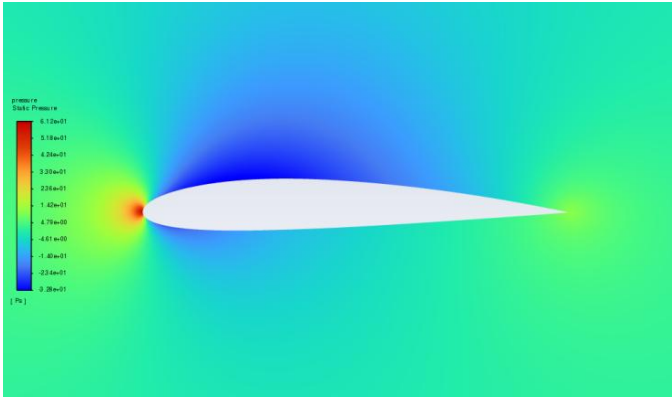


(d)

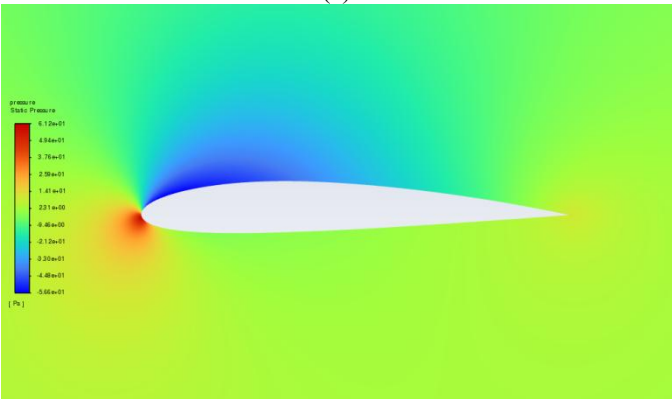


(e)

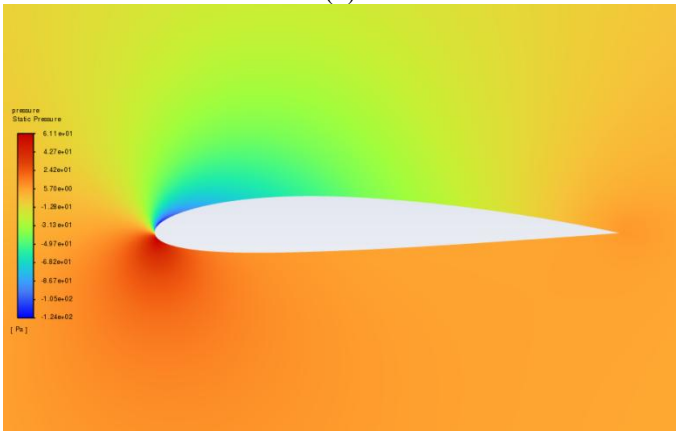
Fig. 7. Pressure distribution cloud maps of NACA2312 at different AOA. (a) 0°; (b) 3°; (c) 6°; (d) 9°; (e) 12°. (Picture credit: Original)



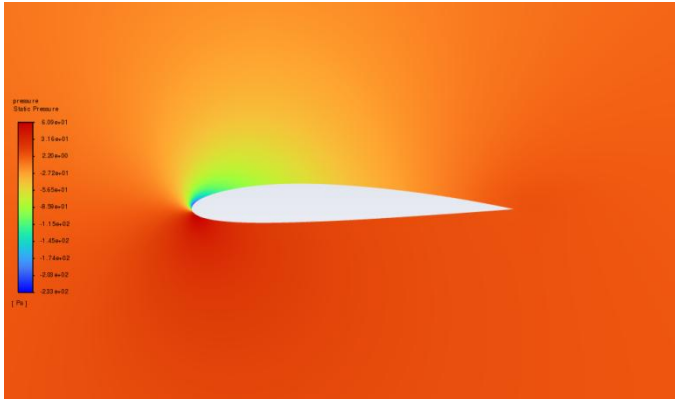
(a)



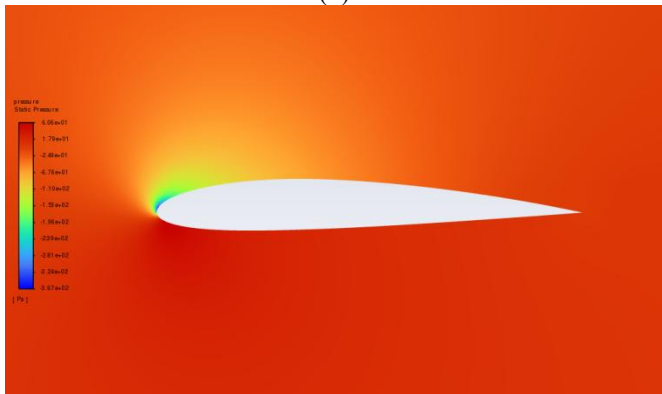
(b)



(c)



(d)



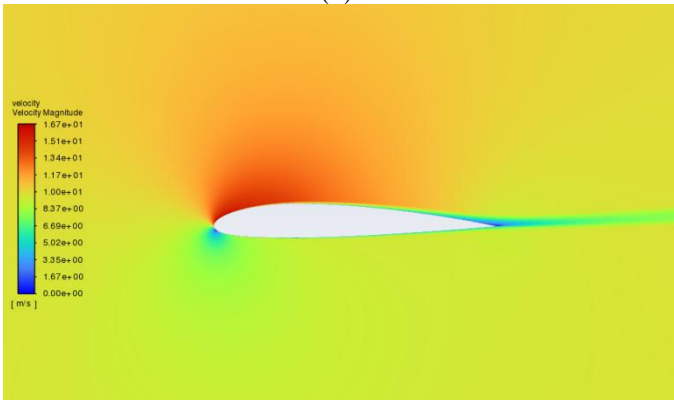
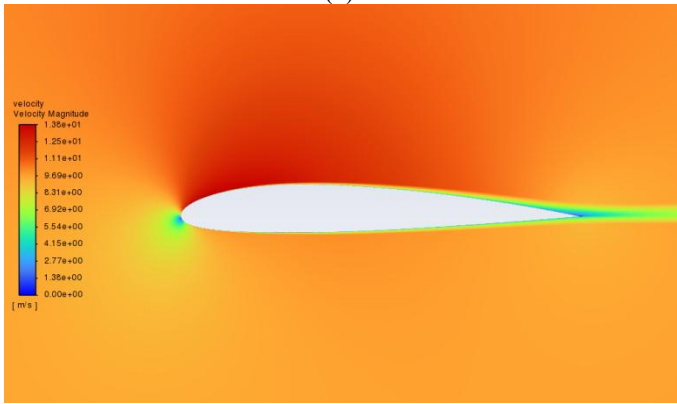
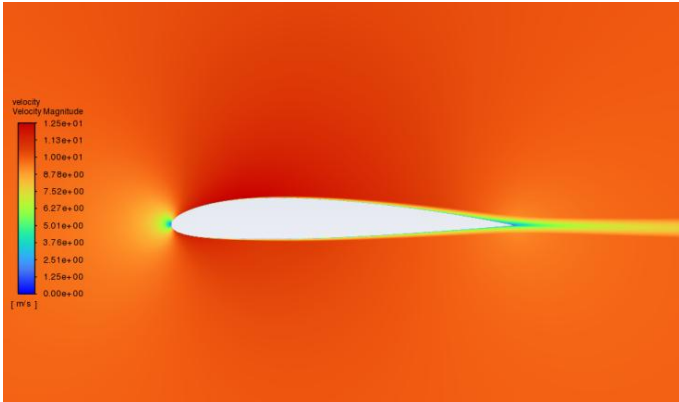
(e)

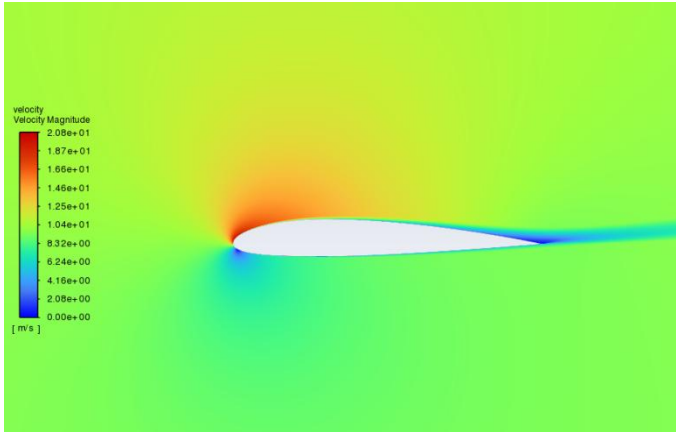
Fig. 8. Pressure distribution cloud map of NACA2412 at different AOA. (a) 0°; (b) 3°; (c) 6°; (d) 9°; (e) 12°. (Picture credit: Original)

In Fig. 9, the separation point of NACA2312 moves forward at high AOA, and the velocity cloud map shows a low-speed region expanding from rear to front.

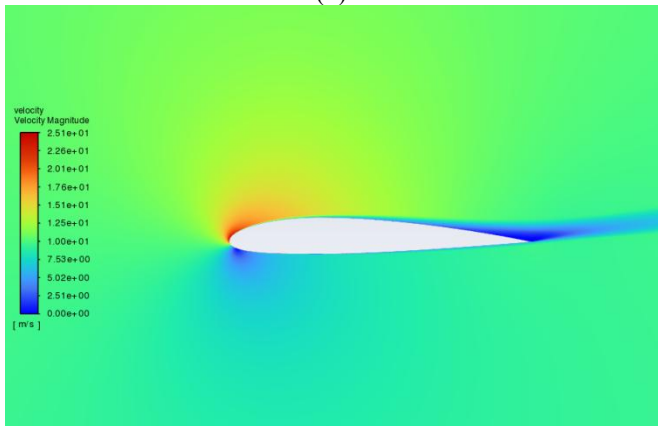
In Fig. 10, the curvature of the middle arc of NACA2412 causes the high-pressure zone to concentrate at the leading edge, and the maximum thickness position affects the flow stability at the trailing edge.

In the velocity distribution cloud map, the velocity variation of NACA2312 is gentle, the separation starts late and has a small range, and the vortex structure is loose. The leading edge acceleration of NACA2412 is significant, with early and intense separation initiation, large vortex scale, and high energy.



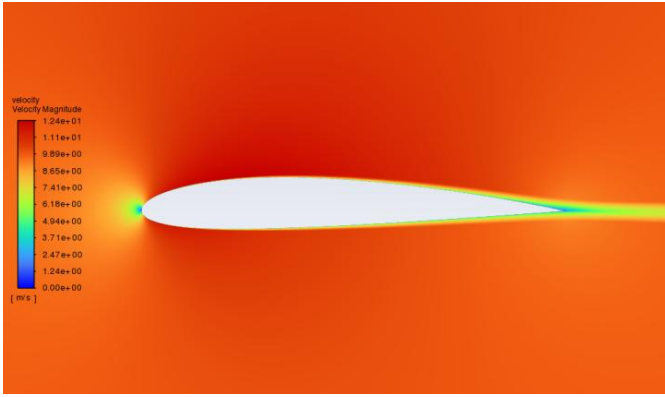


(d)

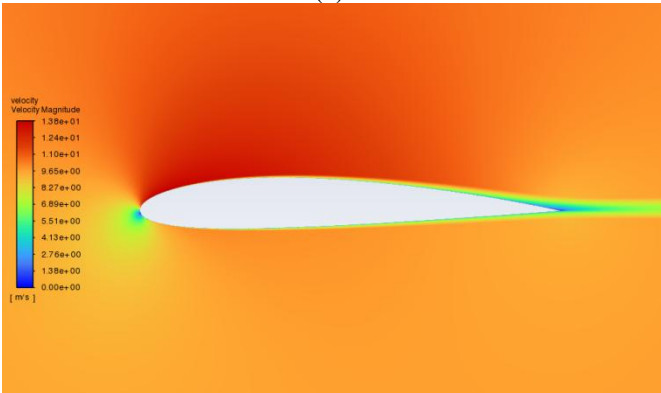


(e)

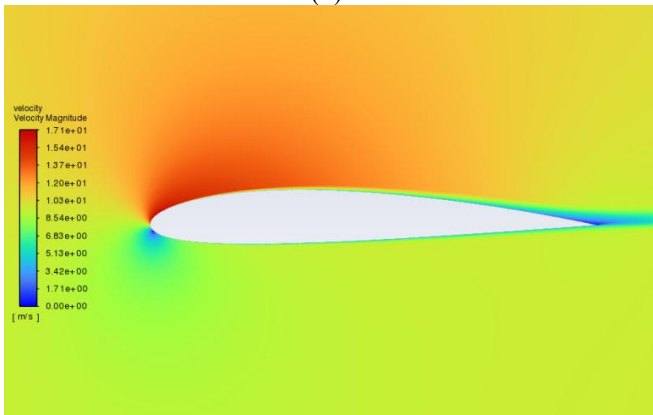
Fig. 9. Velocity distribution cloud maps of NACA2312 at different AOA. (a) 0°; (b) 3°; (c) 6°; (d) 9°; (e) 12°. (Picture credit: Original)



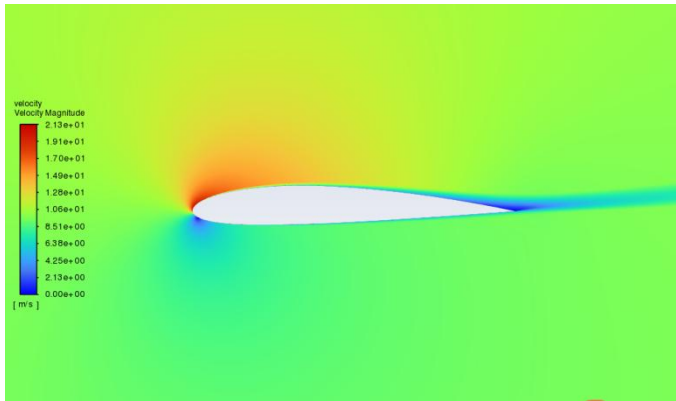
(a)



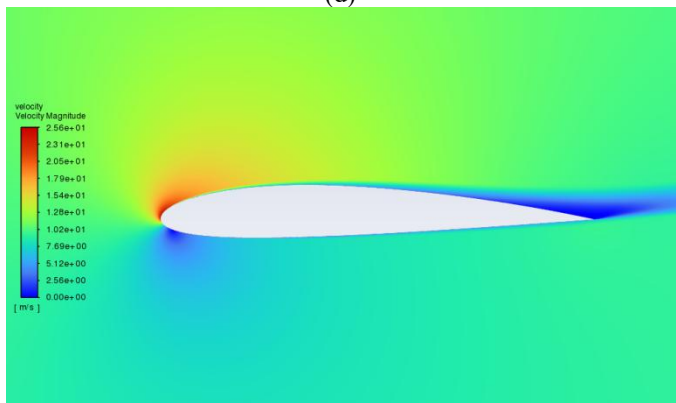
(b)



(c)



(d)



(e)

Fig. 10. Velocity distribution cloud maps of NACA2412 at different AOA. (a) 0°; (b) 3°; (c) 6°; (d) 9°; (e) 12°. (Picture credit: Original)

4 Conclusion

This research uses ANSYS fluent fluid simulation software to simulate the aerodynamic characteristics of two airfoils with different maximum camber positions for comparison. The $K - \omega$ SST model used for simulation under normal air density is generally suitable for the period of aircraft takeoff. What should the speed be when using the $y+$ website to obtain a low Reynolds number, and the final value is 10 m/s. The maximum curvature position will affect the aerodynamic performance of the forward and backward curvature positions. Forward bending can result in low lift but slow surge, making it suitable for designs that require stability and safety as conditions. Backward camber can lead to high lift but severe surge, which entails high maneuverability in scenarios but strict control of the angle of attack. The applicable scenario for this simulation is the aerodynamic performance analysis of aircraft carrying NACA2312 or NACA2412 at different angles of attack at a speed of 10m/s.

The selection of NACA2312 and NACA2412 airfoils in this study has limited reference value for new unmanned aerial vehicles. The main purpose is to supplement the aerodynamic analysis of airfoils in low Reynolds number environments and provide reference suggestions.

References

1. Wei, F., Bai, Y., Zhu, J., etc.: Aerodynamics study of Fsaе tail airfoil. *Mechanical Engineer*, 2024, pp: 61-65
2. Liu, X.: Static and dynamic performance analysis of airfoil at low Reynolds number. *Equipment Manufacturing Technology*, 2016, pp: 55-57
3. Liu, Y., Xia, T., Dong, H., etc.: Research on multi-objective optimization design of low Reynolds number airfoil. *Journal of Nanjing University of Aeronautics and Astronautics*, 2024, pp: 687-697
4. Nordanger, K., Holdahl, R., Kvamsdal, T., Kvarving, A. M., Rasheed, A.: Simulation of airflow past a 2D NACA0015 airfoil using an isogeometric incompressible Navier–Stokes solver with the Spalart–Allmaras turbulence model. *Computer Methods in Applied Mechanics and Engineering*, 2015, pp:183-208.
5. Di, F., Li, L., Li, J., et al.: Full-scale numerical study on the thermal-hydraulic characteristics of steam water separation system in an advanced PWR UTSG. Part two: Droplets separation process, *Progress in Nuclear Energy*, 2020
6. Ahin, Z., Acir, A.: Numerical and Experimental Investigations of Lift and Drag Performances of NACA 0015 Wind Turbine Airfoil .2025
7. Zou, Z., Li, B.: Aerodynamic performance simulation and analysis of naca2412 wing. *China water transport (second half of the month)*, 57, 53-54(2021).
8. Sowmyashree, Y., Aishwarya, D., Spurthy, S., etc. Study on effect of semi-circular dimple on aerodynamic characteristics of NACA 2412 airfoil . *Proceedings of the 2nd International Conference on Emerging Research in Civil, Aeronautical and Mechanical Engineering (ERCAM)*. AIP Publishing LLC. 2019. pp:1-7.
9. Chen, Y.: Numerical simulation and aerodynamic characteristics analysis of external flow field of horizontal axis wind turbine airfoil . MEng thesis. Liaoning University of Engineering and Technology, 2011
10. Yu, C., Wang, X., etc.: Research on the influence of Y+value on the calculation accuracy of airfoil aerodynamic parameters . *Journal of Air Force Engineering University (Natural Science Edition)*, 13, 25-29(2012)

Open Access This chapter is licensed under the terms of the Creative Commons Attribution-NonCommercial 4.0 International License (<http://creativecommons.org/licenses/by-nc/4.0/>), which permits any noncommercial use, sharing, adaptation, distribution and reproduction in any medium or format, as long as you give appropriate credit to the original author(s) and the source, provide a link to the Creative Commons license and indicate if changes were made.

The images or other third party material in this chapter are included in the chapter's Creative Commons license, unless indicated otherwise in a credit line to the material. If material is not included in the chapter's Creative Commons license and your intended use is not permitted by statutory regulation or exceeds the permitted use, you will need to obtain permission directly from the copyright holder.

